Advanced Scientific Instruments xxx (xxxx) xxx

Contents lists available at ScienceDirect

Advanced Scientific Instruments

journal homepage: www.keaipublishing.com/en/journals/asi/

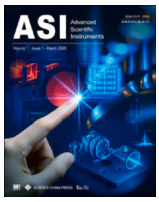

Research Article

A cryogen-free low temperature scanning probe microscope system for ångström-resolved spectroscopic imaging

Ruisong Ma[a,c,1], Zhiwei Liu[b,d,e,1], Dairong Liu[a,c,1], Hao Li[f], Chenshuai Shi[f], Jianfeng Tao[f], Yuanzhi Huang[a,c,g], Li Liu[a,c,f], Zhenchao Dong[b,d], Bing Wang[b,d,e], Shijing Tan[b,d,e,*], Qing Huan[a,c,f,g,*]

[a] Beijing National Center for Condensed Matter Physics and Institute of Physics, Chinese Academy of Sciences, Beijing 100190, China
[b] Hefei National Research Center for Physical Sciences at the Microscale and Synergetic Innovation Center of Quantum Information and Quantum Physics, University of Science and Technology of China, Hefei 230026, China
[c] Beijing Key Laboratory of Atomic-scale Manufacturization and Advanced Vacuum System, Beijing 100190, China
[d] Hefei National Laboratory, University of Science and Technology of China, Hefei 230026, China
[e] New Cornerstone Science Laboratory, University of Science and Technology of China, Hefei 230026, China
[f] ACME (Beijing) Technology Co., Ltd., Beijing 101407, China
[g] School of Physical Sciences, University of Chinese Academy of Sciences, Beijing 100190, China

ARTICLE INFO

Key words:
Cryogen-free
Remote liquefaction scheme
Scanning probe microscopy
Tip-enhanced Raman spectroscopy

ABSTRACT

We report the development of a cryogen-free, low-temperature optical-coupled scanning probe microscope (LT-OC-SPM) designed for high-resolution multimodal imaging and spectroscopy. To mitigate the mechanical vibrations from the cryocooler cold head, we implement a remote liquefaction scheme that effectively decouples the noise from the tunneling junction. The system achieves a stable base operation temperature below 3 K and a tunneling current noise level under 20 fA/Hz$^{1/2}$, comparable to the performance of the conventional SPM systems employing bath cryostats. Moreover, our system features a customized rigid scanner integrated with in-vacuo piezo-driven high-numerical aperture lenses, facilitating simultaneous topographic and spectroscopic measurements. Multimodal characterization of silver phthalocyanine (AgPc) molecules on Ag(110) demonstrates ångström scale probing of intramolecular structure and localized vibrational modes, highlighting the versatility of our system in high-resolution surface characterization. Consequently, this remote liquefaction architecture provides a sustainable, high-performance cryogen-free platform for ångström-resolved spectroscopic imaging, establishing a robust foundation for future multifunctional near-field optical spectroscopy.

1. Introduction

Recent advances in condensed matter physics, quantum science, and nanotechnology have driven a critical demand for techniques that can characterize and manipulate surfaces at the nanoscale.[1] Multimodal ultra-high vacuum (UHV) scanning probe microscopy (SPM) systems, which integrate scanning tunneling microscopy (STM) and atomic force microscopy (AFM), have emerged as essential tools in these fields.[2,3] These systems enable nanoscale morphology imaging,[4] mapping of localized electronic properties,[5] and single-atom manipulation,[6] demonstrating exceptional versatility. However, conventional SPM lacks direct chemical identification capabilities. To overcome this obstacle, SPM-based near-field optical spectroscopy, such as tip-enhanced Raman spectroscopy (TERS) and STM-induced luminescence (STML), has been developed.[7,8] Merging the spatial resolution of SPM with the chemical sensitivity of optical spectroscopy, these hybrid techniques enable analysis with extreme spatial confinement. They have thus been applied to study molecular identity,[9–11] single-bond dynamics,[12–14] inter- and intra-molecular energy transfer,[15–17] structure–property relationships,[18–20] two-dimensional (2D) materials,[21–23] etc. Even though nanoscale resolution is achievable with external lenses, the relatively high noise pickup and low photon collection efficiency of such setups have hindered their performance.[24] To address these drawbacks, internally optical-coupled SPM (OC-SPM) systems have been developed,

* Corresponding authors
E-mail addresses: tansj@ustc.edu.cn (S. Tan), huanq@iphy.ac.cn (Q. Huan).
[1] These authors contributed equally to this work

https://doi.org/10.1016/j.asi.2026.100011
Received 5 February 2026; Received in revised form 23 February 2026; Accepted 26 February 2026

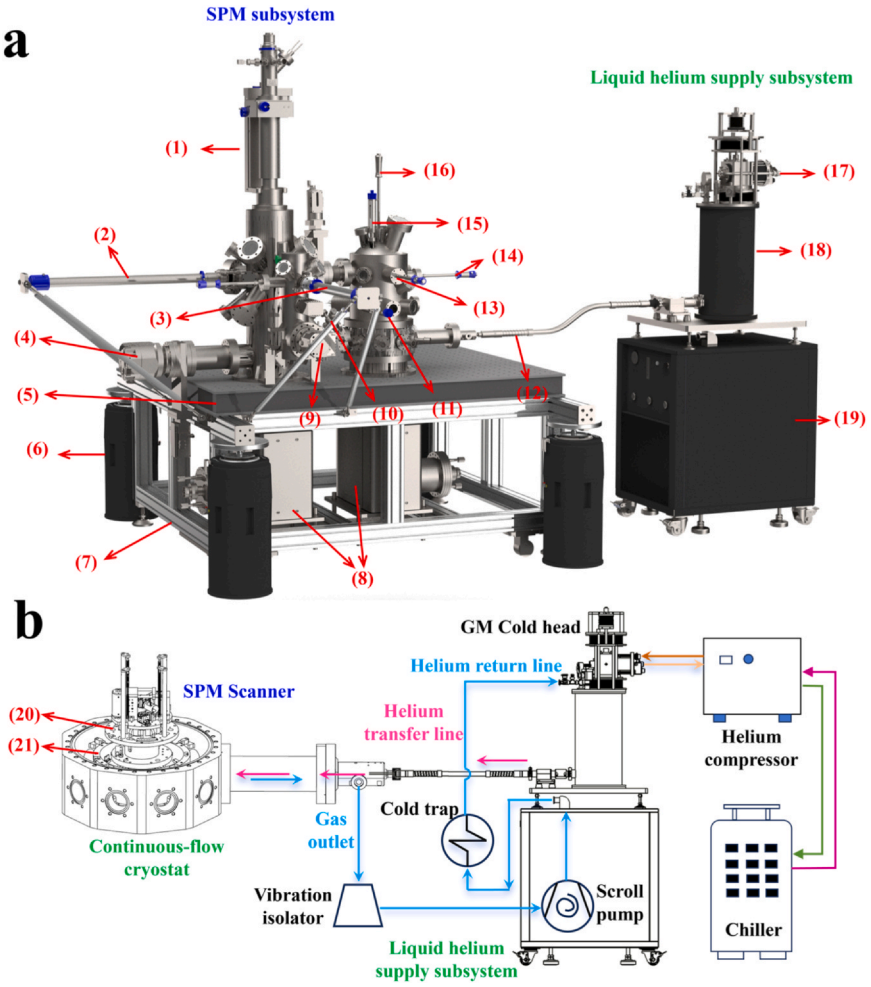

Fig. 1. 3D model and schematic diagram of the cryogen-free LT-OC-SPM system. (a) Isomeric view of the entire system. (b) Schematic diagram of the circulation of the cryogen-free OC-SPM system. Notably, the figures are not drawn to scale. (1) Four-axis manipulator; (2) Magnetic rod for transferring dock in the preparation chamber; (3) Transfer rod in the load-lock chamber; (4) 300 L/s turbo pump; (5) Honeycomb breadboard; (6) Pneumatic legs; (7) Aluminum profile frame; (8) Sputtering ion pump; (9) 85 L/s turbo pump; (10) Ion source; (11) Linear driver for the light and dosing shutter control, (12) Helium transfer line; (13) Magnetic rod for dock; (14) Magnetic rod for transfer window motion; (15) Linear driver for clamp control; (16) Wobble stick for sample and tip exchange; (17) GM Cold head; (18) Liquefying chamber; (19) Gas handling system; (20) Cold finger plate; (21) Outer shield plate.

incorporating in-chamber lenses mounted directly on or near the scanner.[25–29] In such systems, 3D nano-positioner-driven optics are precisely aligned to the tip, making OC-SPM a crucial implementation for high-resolution near-field spectroscopy.[30]

Although room-temperature setups show flexibility in operation, the superior stability of cryogenic environments is essential for sub-nanoscale precision.[31,32] Consequently, liquid-helium-based low-temperature (LT) OC-SPM (< 6 K) has emerged as a platform enabling high-resolution imaging and spectroscopy.[33] However, conventional LT-OC-SPM systems rely on bath[34,35] or continuous-flow cryostats,[36,37] both of which are dependent on liquid helium. This reliance presents a major challenge due to the rising cost and supply volatility in global helium markets. Moreover, the finite holding time of liquid helium constrains experimental duration. Given that tip shaping and optical alignment in OC-SPM are significantly more time-consuming than in standard SPM experiments, these logistical and economic constraints severely limit data acquisition time, prompting a search for cryogen-free alternatives.[38] In response, closed-cycle architectures with Gifford-McMahon (GM)[39,40] or pulse tube (PT)[41,42] cryocoolers have been used to cool the SPM system to near or below 4 K. However, most designs typically involve loading the cryocooler directly on top of the SPM chamber, which introduces significant mechanical vibrations that are challenging to decouple and occupies a large spatial footprint.[43] These drawbacks are particularly detrimental for OC-SPM, where optical elements are highly sensitive to vibration and require substantial physical clearance.

Recently, we reported a sub-3 K cryogen-free platform utilizing a remote liquefaction scheme to optimize vibration isolation and spatial efficiency.[44] In this work, we advance this architecture into a fully operational LT-OC-SPM system. The design integrates a horizontally mounted continuous-flow SPM cryostat for LT-SPM with liquid helium supplied by a GM cryocooler-based remote liquefying chamber. The liquid helium is delivered via a vacuum-jacketed flexible transfer line while the exhaust gas is returned to the liquefying chamber through vibration-damped pipelines. This compact, integrated architecture provides sufficient spatial clearance for optical elements. The cooling performance test confirms a stable base temperature of the scanner, which features dual 3D nano-positioners and high-numerical aperture (NA) aspheric lenses, achieving a total photon collection efficiency of ~22.8%. The vibration-isolated architecture ensures ultra-low noise operation, facilitating atomic resolved STM, non-contact AFM (nc-AFM), as well as high-resolution scanning tunneling spectroscopy (STS, dI/dV *vs.* V) and near-field optical spectroscopy. Furthermore, we validate these multimodal capabilities through a systematic study of silver phthalocyanine (AgPc) on Ag(110), demonstrating ångström-scale structural and spectroscopic imaging in our system. Consequently, the current research demonstrates that the remote liquefaction scheme provides a robust, high-performance foundation for cryogen-free, multimodal SPM systems, enabling continuous operation over several months.

2. System overview

The cryogen-free LT-OC-SPM developed in this work comprises two primary subsystems: a continuous-flow cryostat-based SPM subsystem and a GM cryocooler-based helium supply subsystem. This section details the structural and functional design. The optical-coupled

multimodal scanner and the integrated optical setup are also presented, which are pivotal for achieving high-resolution near-field optical spectroscopy while maintaining an ultra-low vibration environment.

2.1. SPM subsystem

As illustrated in Fig. 1a, the SPM subsystem is supported by an aluminum profile frame, which incorporates an optical breadboard for holding the optical elements. Four pneumatic legs (Newport, S-2000A) are used to lift the frame and isolate it from ground vibrations when necessary. The subsystem comprises three chambers: a load-lock chamber, a preparation chamber, and an SPM chamber. The load-lock chamber is equipped with a magnetic rod with eight docking positions for storing sample and tip holder plates. A long transfer rod transports the holders between the load-lock and the preparation chamber. In the preparation chamber, a six-position storage dock mounted on a magnetic transfer rod enables the delivery of plates to the SPM chamber. Sample treatment is performed using a customized top-mounted 4-axis manipulator, supporting resistive heating (>500°C), electron-beam heating (>1000°C), and direct current flashing (>1200°C) of the sample. In addition, cryogenic cooling of the sample in the manipulator to below −150°C is also available via liquid nitrogen flow. For surface cleaning and sample preparation, the preparation chamber is equipped with an Ar^+ ion source (ACME, ISE35) for sputtering and multiple on-axis flanges for mounting evaporators.

The SPM chamber features a magnetic rod with a ten-position dock. The sample and tip transfer between this dock and the scanner is facilitated by a customized wobble stick mounted atop the chamber. A dedicated transfer window is actuated by a side-mounted magnetic rod, as shown in Fig. 1a. Two linear drivers, located at the top and side of the chamber, control the scanner clamp and internal shutters, respectively. The cooling capability is provided by a compact continuous-flow cryostat (Physike Tech., PHY-Scryo-S200) mounted laterally to the SPM chamber, which cools a central cold finger plate to <3 K using liquid He from the liquifying chamber. The exhaust gas from the cold finger plate is subsequently routed to cool the outer shield plate to tens of Kelvin. The radiative heat load is minimized by nested thermal shielding, consisting of an inner shield attached to the cold-finger plate and an outer shield mounted to the outer-shield plate. This dual-layer shielding system includes synchronized interlocking ports for sample transfer, optical access, and *in-situ* dosing, which are shuttered during SPM measurements to minimize the thermal leakage. Inside the inner shield, a modified pan-type scanner[45] (detailed in the following section) is suspended by four tension springs and an eddy-current damping unit, which comprises six SmCo magnets on the cold finger plate. Thermal equilibrium between the scanner and the cold finger plate is maintained via several spiral copper braids, while a 50 Ω resistive cartridge heater enables variable-temperature operation. The temperatures of the cold finger plate, outer shield plate, and sample stage are monitored using calibrated zirconium oxynitride sensors (Physike Tech., ZrON-10).

To minimize signal crosstalk and noise pickup, wiring schemes differ for distinct signal types. The tunneling current (I_t), bias voltage (V_{bias}), and nc-AFM signals are routed from the scanner to the cold finger plate via silver-plated alloy coaxial cables, followed by stainless steel coaxial lines to the vacuum chamber feedthroughs. Simultaneously, control and readout signals for the piezo actuators, 3D nano-positioners, temperature sensors, and heater are carried by twisted-pair manganin wires. All wiring is thermally anchored to both the cold finger plate and the outer shield plate to ensure effective heat sinking.

The system supports rapid tip exchange for different experimental modalities. In this research, the mechanically cut Pt-Ir tips, the electrochemically etched Ag tips,[46] and the customized qPlus AFM sensors with W tips are used. Detailed specifications are provided in the following section. The I_t signal is amplified by a room temperature current preamplifier (ACME, IVC100), while the nc-AFM signal is amplified using an LT AFM preamplifier (ACME, AMP100). All these signals are transmitted to a Nanonis SPM controller with a lock-in module (SPECS GmbH), and the recorded data is processed using WSxM software.[47] The temperature signal is recorded by a commercial multi-channel controller (Physike Tech., 24 C).

A stage pumping architecture achieves and maintains a UHV environment for the system. Initial evacuation is handled by a 300 L/s turbomolecular pump (Edwards, nEXT300D) on the preparation chamber and an 85 L/s pump (Edwards, nEXT85H) on the load-lock, both of which are connected to a forepump (Edwards, nXDS6i). The base pressure below 8×10^{-9} mbar in the load-lock chamber can be achieved. For ultimate vacuum, the preparation and SPM chambers are each equipped with a sputtering ion pump (SKY Tech., SIP400AF), which features integrated titanium sublimation and ion getter modules. They sustain the base pressure of $<2 \times 10^{-10}$ mbar in both chambers. All three chambers are isolated by gate valves to ensure independent pressure management and prevent cross-contamination.

2.2. Cryogen-free helium supply subsystem

The cryogen-free helium supply subsystem is based on a dual-loop closed-cycle architecture, as illustrated in Fig. 1b. The primary loop circulates helium between a GM cryocooler (Sumitomo, SRDE-418) and its compressor (Sumitomo, F-50), cooling the GM cold head into the liquid helium temperature regime. The second loop, hereafter referred to as the main He circulation loop, is driven by a dry scroll pump (Edwards, nXDS15iR) within the gas handling system. In this main loop, helium gas undergoes successive heat exchange with the two stages of the GM cold head, reaching a pre-cooled state below 8 K. The gas is liquefied into a superfluid state via a needle-valve-controlled throttling process[48] and subsequently delivered through a flexible transfer line to the continuous-flow cryostat, cooling the cold finger plate to below 4 K. The exhaust He gas flows out of the cryostat along the He return line and is pumped back into the liquefying chamber to close the loop. The vibration from the pump is isolated by sandwiching the return pipeline with an isolator made of a stainless-steel block. Notably, while conventional cryocooler cold heads generally necessitates a near-vertical installation, the remote liquefaction scheme offers the flexibility of arbitrary 360° mounting.[44] In our system, a horizontal orientation is specifically designed to provide the necessary spatial clearance for the integrated optical assembly. Moreover, to further reduce the transmission of mechanical vibration from the GM cryocooler, the GM cold head is levitated and mounted on the liquefying chamber with three bellows in a self-balanced configuration. Comprehensive details regarding the control principles, vibration isolation, and gas handling logic are provided in our previous work.[44]

2.3. Optical-coupled scanner

To achieve the precise focus alignment and specific polarization required for near-field optical spectroscopy, we developed an optical-coupled scanner featuring integrated in-vacuo lenses. As shown in Fig. 2a, the assembly is mounted on a molybdenum baseplate equipped with magnets for eddy-current damping. Moreover, adapted from a previously reported perpendicular design configuration,[33] the scanner features a horizontal tip orientation that streamlines external beam steering and alignment.

Two customized 3D nano-positioners, each comprising a stacking of three modified pan-type piezoelectric steppers, are assembled symmetrically on either side of the tip to provide travel ranges of 4 mm (X/Y) and 8 mm (Z), as shown in Fig. 2a. In this configuration, the X-stepper handles horizontal motion (parallel to the ground), the Y-stepper provides vertical movement (perpendicular to the ground), and the Z-stepper controls the focus along the optical axis. Each nano-positioner carries an aspherical lens with an NA of 0.46, providing a total photon collection efficiency of about 22.8% with dual lenses (see the details in supporting information). To ensure mechanical stability and prevent

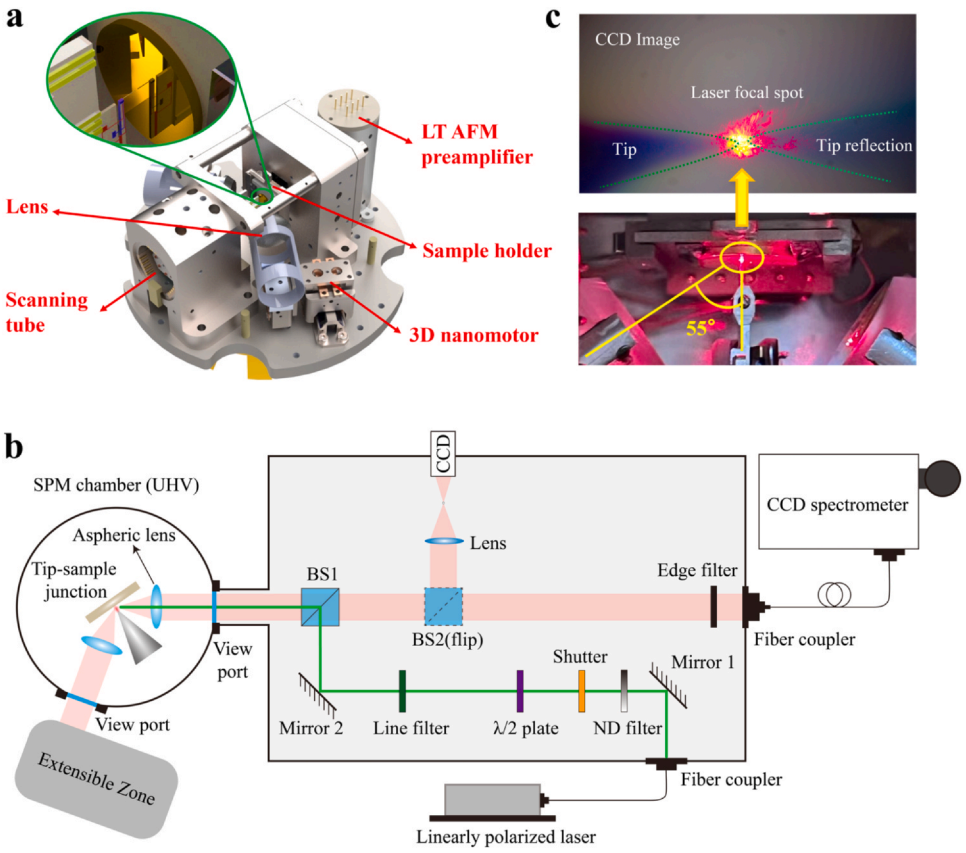

Fig. 2. Design of the OC-scanner and optical integration. (a) 3D model of OC-scanner with the main elements marked. The inset image shows the tip-sample junction with a qPlus AFM sensor. (b) Schematic diagram of the home-built optical system. (c) Photographs of the 633-nm laser focused on the tunneling junction. The bottom photo is taken by an external camera, while the upper image is acquired with the CCD camera inserted into the optical path.

vertical overloading, the *Y*-stepper is mounted atop the *X-Z* assembly. Notably, to maximize the plasmonic enhancement for tip-enhanced spectroscopy,[49] the optical axes are set at 55° relative to the tip apex. All the light ports and corresponding chamber viewports are coaxially aligned with the optical axis to ensure an unobstructed path. This rigid, compact design operates reliably at 4 K temperatures, ensuring high collection efficiency without introducing parasitic mechanical noise to the tunneling junction.

Moreover, to mitigate noise from parasitic cable capacitance,[50] a LT AFM preamplifier is integrated directly onto the scanner within a dedicated shield. This proximity significantly reduces the distance between the qPlus AFM sensor and the first stage of amplification, thereby optimizing the signal-to-noise ratio of nc-AFM measurements.

2.4. Optical setup

The STML and TERS measurements were conducted using a custom-designed optical assembly, which is schematically shown in Fig. 2b. Although the scanner features nano-positioner-driven lenses on both sides, excitation and collection were carried through the same side in this research, leaving the opposite lens available for extensive setup (e.g., a second camera for 3D alignment or a single-photon counter for precision measurement). By taking advantage of the compact, horizontal architecture of the remote liquefaction system, optical elements can be mounted in proximity to the vacuum chamber. This configuration minimizes optical path lengths, effectively mitigating intensity attenuation for both the excitation laser and the emitted signal. Mechanical stability and coaxial alignment are strictly maintained by mounting all optical elements on a dark box system, which is attached to the chamber viewport via an adapter.

On the excitation side, the laser beam is introduced from the fiber coupler at the side of the box. The laser beam first passes a neutral density filter (ND filter) for controlling the laser power, preventing damage to sensitive samples from high-intensity incident light. Next, to ensure proper polarization, the laser beam is aligned using a half-wave plate to match the excitation polarization with the tip apex.[51] A line filter then allows the light with the desired wavenumber to pass, narrowing the spectrum of the incident light. The beam is subsequently directed by a 3 : 7 (R : T) beamsplitter (BS1) through the viewport and focused onto the tip–sample junction via a nano-positioner-positioned aspheric lens (f = 12.4 mm, NA = 0.46).

Signal collection follows a confocal geometry, where photons are collected by the same aspheric lens and transmitted through BS1. For TERS measurements, the signal then passes through an edge filter. Specifically, for Stokes Raman, a longpass filter is used here to filter out reflected light, Rayleigh-scattered photons, and anti-Stokes Raman scattering. Conversely, for anti-Stokes Raman detection, a shortpass filter can be used. In the case of STML, the edge filter is removed from the optical path to maximize broadband photon collection. Finally, the photons are focused into an optical fiber and directed to a CCD spectrometer (Princeton Instruments, SpectraPro HRS-300). To evaluate the laser focusing at the tunneling junction and enable three-dimensional alignment of the aspheric lens, a flippable beamsplitter (BS2) is inserted into the optical path to divert part of the beam to a CCD camera (Pixelink, PL-D795CU). During optical signal acquisition, BS2 is flipped out of the beam path to maximize photon collection efficiency.

This optical configuration delivers both precision and modular versatility. As demonstrated in Fig. 2c, the laser (633 nm, Crystalaser, DL633-050-SO) focal spot coincides perfectly with the junction between the tip and its optical reflection, confirming accurate focusing within the tunneling junction. The fiber-coupled input enables rapid exchange of excitation lasers, while the cage architecture allows the entire optical unit to be detached and reinstalled without requiring realignment. These design features significantly streamline experimental workflows and ensure high reproducibility.

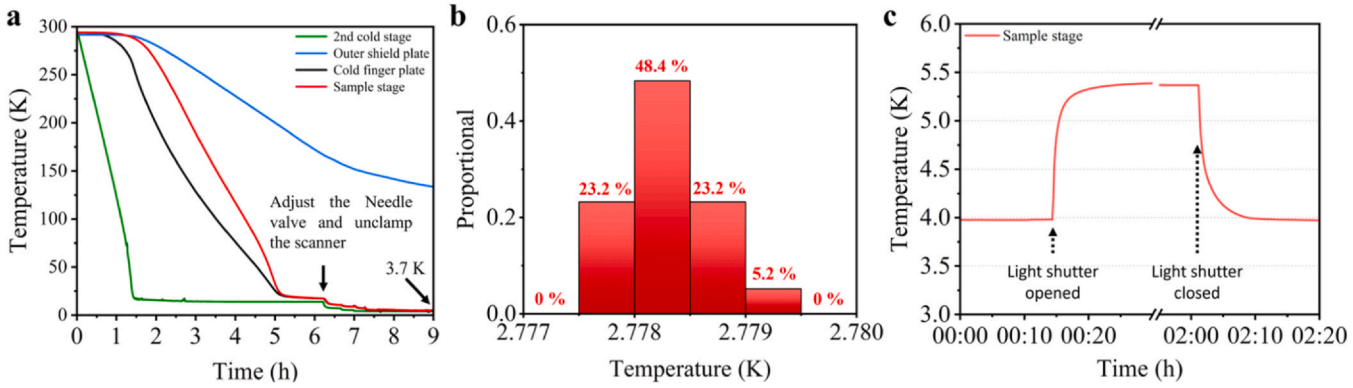

Fig. 3. Cooling performance and temperature stability of the cryogen-free OC-SPM system. (a) Cooldown curves for the second cold stage of the GM cryocooler, the outer shield, the cryostat cold plate, and the scanner sample stage. The sample stage cools to below 10 K in ~6.2 h and below 4 K in ~9 h. (b) Temperature histogram measured at the sample stage over 1 h after the base temperature of 2.778 K was reached. The temperature fluctuates within ±1 mK over one hour. (c) Temperature variation with the light shutter opened and closed.

3. Results and discussion

The performance of the LT-OC-SPM was first demonstrated by recording its cryogenic metrics (cooldown rate and stability) and power spectral density (PSD) of the tunneling current. Its characterization capabilities were further validated through high-resolution STM, nc-AFM, STS, STML and TERS measurements.

3.1. Cooling performance and temperature stability

The cooling performance was evaluated by the cooling-down curve, base temperature, and thermal stability. As shown in Fig. 3a, the scanner reaches 10 K from room temperature within 6.5 h. Following the optimization of the needle valve and the unclamping of the scanner, the sample stage cools below 4 K within an additional 3 h. A further ~10 h of overnight stabilization is then required to eventually reach the ultimate base temperature of 2.778 K. At this base temperature, the system exhibits exceptional stability, with fluctuations restricted within ±1 mK over one hour. This negligible deviation confirms the high thermal stability required for high-resolution, long-duration measurements.

While an ultimate base temperature of <3 K is achievable with all radiation shutters closed, reaching thermal equilibrium at this limit requires a prolonged stabilization period. Consequently, to optimize experimental throughput, practical experiments are typically conducted at temperatures below 4 K regime. Additionally, as shown in Fig. 3c, opening the light shutter for laser excitation and signal collection introduces a significant radiative thermal load, increasing the sample temperature to approximately 5.4 K. Upon closing the shutters, the temperature recovers to below 4 K within 10 min, demonstrating the high efficiency of the thermal anchoring and management within the scanner assembly (more details please find Fig S1 in supporting information).

3.2. PSD measurement

As SPM and near-field optical spectroscopy operate with atomic-scale precision, they are acutely susceptible to mechanical disturbances, making robust vibration isolation a fundamental requirement for LT-OC-SPM performance. To evaluate system stability, the PSD of the tunneling current in the range of 1–1000 Hz was measured at 4 K under three conditions: tip withdrawn, engaged with feedback off, and engaged with feedback on. As shown in Fig. 4, the withdrawn tip indicates a base noise below 10 fA/Hz$^{1/2}$. Under typical operating conditions (feedback on), the noise level remains approximately 20 fA/Hz$^{1/2}$, comparable to conventional SPM systems employing liquid-helium bath cryostats. The state of tip engaged with feedback off yields a noise

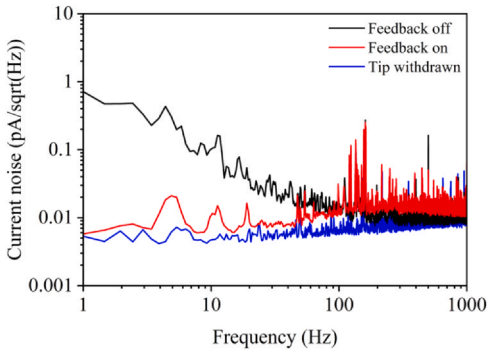

Fig. 4. The PSD of tunneling current obtained at 4 K with a mechanically cut Pt-Ir tip and Au(111) sample. Tunneling condition: I_t = 100 pA, V_{bias} = −100 mV.

density below 1 pA/Hz$^{1/2}$, confirming high-resolution stability. Distinct peaks between 3–10 Hz and near 20 Hz are attributed to the pneumatic legs and copper thermal braids, respectively, while interference at 50 Hz and 100–200 Hz originates from the operating mechanical and turbo pumps. The consistently low noise level, despite active pumping, underscores the robust mechanical and acoustic isolation of the system.

3.3. STM and STS performance

The STM and STS performance of the system was characterized using a clean Au(111) surface prepared by cycles of Ar^+ sputtering and subsequent annealing. Atomically resolved imaging (Fig. 5a) reveals a well-ordered hexagonal lattice with a measured lattice constant of 2.90 Å, determined via line-profile analysis (Fig. 5b). This value is in excellent agreement with the literature (2.89 Å),[52] confirming the high spatial precision of the system. Furthermore, STS measurements on the same surface capture the characteristic Au(111) surface-state onset near −420 mV, which matches well with reported values.[53]

3.4. Nc-AFM performance

As depicted in the previous section, an LT AFM preamplifier was mounted directly on the scanner to minimize capacitive noise pickup. To evaluate the effectiveness of this configuration, nc-AFM measurements were performed using a customized qPlus AFM sensor with an electrochemically etched W tip mounted on the free prong of the fork (Fig. 6a).[54] Frequency sweep analysis (Fig. 6b) reveals a resonant frequency of ~30.5 kHz with a quality factor (Q) of ~84,000. The performance of the qPlus AFM setup is demonstrated by probing a bilayer NaCl film grown on Au(111), which was prepared via a resistive

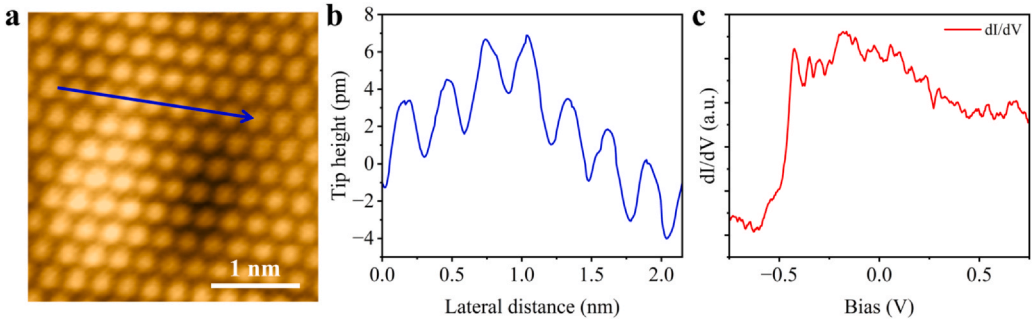

Fig. 5. STM and STS measurement of clean Au(111) surface. (a) Atomically resolved constant current STM image of the clean Au(111) surface using a Pt-Ir tip. I_t = 834.9 pA, V_{bias} = −80.9 mV. (b) Profile of the tip height along the line marked in (a). (c) STS spectra acquired with a qPlus sensor using a W tip. I_t = 100 pA, V_{bias} = −2 V, the amplitude (V_{mod}) and frequency (f_{mod}) of the modulation bias are 10 mV and 973 Hz.

heating evaporation (ACME, RHE35A). The sample was first characterized in STM mode (Fig. 6c) and subsequently imaged in constant-height nc-AFM mode (Fig. 6d). The clear atomic lattice resolved in the nc-AFM image, precisely aligned with the STM topography, validates the low-noise performance of the integrated preamplifier design and the overall mechanical stability of the system.

3.5. STML performance

To assess the optical performance of our system, we performed STML on a clean Ag(110) surface using an electrochemically etched Ag tip. The tip was held with I_t = 8 nA and V_{bias} = 3 V to excite highly localized emission, which is known to arise from the radiative decay of the nanocavity plasmon excited by inelastic tunnelling electrons. Given that the resonance features depend sensitively on the apex shape and size of the tip, a series of spectra (10 s acquisition time for each) are obtained via shaping the tip during the STML measurements. The acquired spectrum (Fig. 7) exhibits distinct emission bands in the 500–800 nm range, consistent with the characteristic localized plasmon resonances reported for Ag-Ag junctions.[46,55] Despite the distinct features, all the spectra exhibit well-defined spectral profiles and a high signal-to-noise ratio, demonstrating the superior spectroscopic resolution and photon collection efficiency of our optical assembly. These findings confirm the excellent compatibility and sensitivity of our setup for nanoscale optical experiments and for detecting weak emissive processes under cryogen-free conditions.

3.6. Multimodal characterization of AgPc on Ag(110) substrate

The primary advantage of our system lies in the synergy between the integrated multimodal scanner and the cryogen-free refrigeration architecture. The scanner facilitates comprehensive, correlative measurements on a single sample, while the cryogen-free design ensures the long-term thermal and mechanical stability required for complex, extended experimental workflows. To demonstrate these capabilities, we performed a systematic characterization of AgPc molecules adsorbed on an Ag(110) surface using STM, STS, nc-AFM, and TERS.

Sample preparation was conducted by thermally evaporating the phthalocyanine (H_2Pc) molecules onto a precleaned Ag(110) surface via a home-built evaporator, followed by post-deposition annealing to 350°C. Large-scale STM imaging (Fig. 8a) reveals isolated adsorbates with two distinct configurations. The four-lobe structures (circled out by red rings) are identified as deprotonated H_2Pc (central H atoms removed), where each lobe corresponds to an isoindole unit.[56] Meanwhile, the cross-like structures (circled out by yellow rings) indicate a chemical transformation. To elucidate the atomic structure of this species, high-resolution STM and nc-AFM were performed using a CO-functionalized tip (Fig. 8b, c). While STM reveals a distinct protrusion at the molecular center, nc-AFM resolves this feature as a single atom bonded to the nitrogen atoms of the four isoindole units. This structural evidence confirms the formation of AgPc via the self-metalation of H_2Pc during the annealing process (Fig. 8d).[57,58]

Next, the STS measurement was conducted on the molecular lobes and the bare Ag surface (Fig. 8e) to verify the electronic properties of AgPc. The spectra reveal distinct peaks corresponding to the highest occupied molecular orbital (HOMO) and the lowest unoccupied molecular orbital (LUMO) at −0.5 and 0.5 V, respectively. Furthermore, dI/dV mapping at these bias voltages visualizes the spatial distribution of the HOMO and LUMO states, demonstrating an ångström scale probing of the intramolecular electronic properties.

Furthermore, to complement the structural data with chemical fingerprints, TERS measurements were performed with an Ag tip (Fig. 8g).

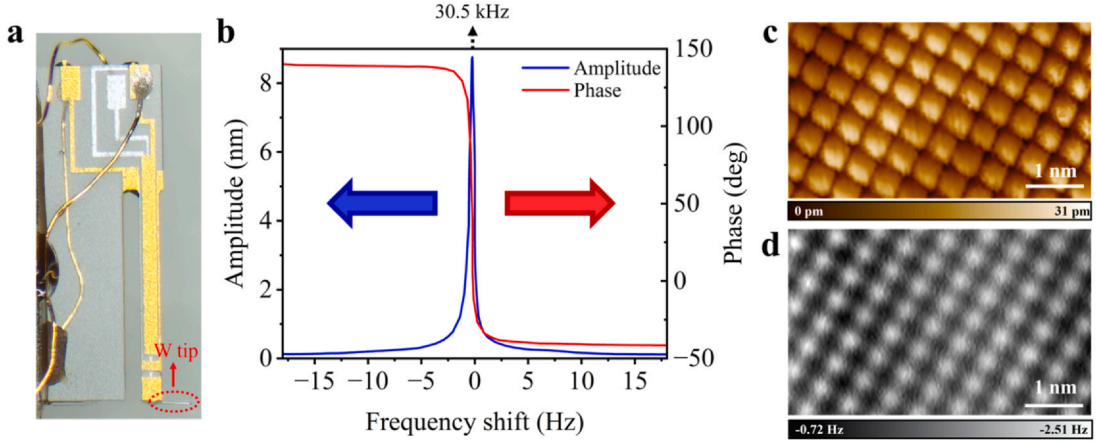

Fig. 6. AFM measurement on NaCl/Au(111) sample. (a) Photograph of a qPlus sensor used in this research. The W tip is marked out by the red dashed ellipse. (b) Sweeping frequency curve of a qPlus sensor, the frequency with the highest amplitude is about 30.5 kHz, which is marked as the resonance frequency of the sensor. A typical Q value of ~84,000 can be extracted from the phase and frequency sweep. (c) STM image of a bi-layer NaCl film. I_t = 171.2 pA, V_{bias} = −20.1 mV. (d) Constant-height AFM image of the same area in (c), AFM oscillation amplitude = 1 nm.

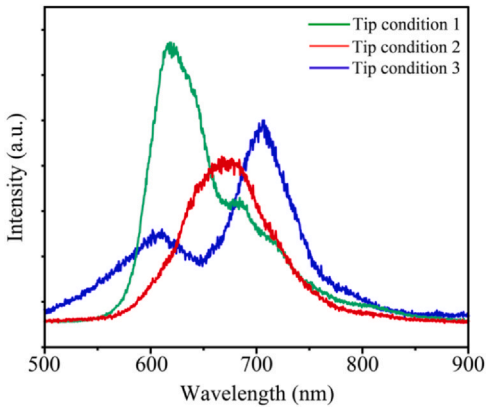

Fig. 7. STML spectrum collected with electrochemically etched Ag tip. I_t = 8 nA, V_{bias} = 3 V, 10 s acquisition time for each spectrum. Three distinct resonances are observed after shaping the same tip on the Ag surface, indicating the sensitivity of resonance features towards the tip conditions.

A featureless spectrum acquired on the bare Ag surface (black) confirms the cleanliness of the tip for TERS measurement. In contrast, some characteristic Raman peaks are detected upon placing the tip on the gap (red), lobe (blue), and center (green) of the molecule (5 nA, 0.1 V, t_{acq} = 40 s), suggesting the vibrational modes of the AgPc molecule. Importantly, while several vibrational modes are uniform across the molecule, certain characteristic peaks exhibit position-dependent intensities, reflecting the spatial distribution of distinct vibrational normal modes. This intramolecular spatial variation of vibrational modes is characterized by TERS mapping (Fig. 8h, 6 nA, 0.1 V, 20 × 20 pixels, t_{acq} = 2 s/pixel).

Simultaneously, the concurrently acquired STM topography (Fig. 8i) is used to precisely determine the molecular position and to ensure negligible spatial drift. The TERS mapping image of mode I (389 cm^{-1}) is tentatively proposed to be a macrocycle-dominated out-of-plane breathing-like deformation mode that emerges upon Ag coordination to the pyrrolic N_4 core. Therefore, the mode I exhibits a relatively uniform spatial distribution. Whereas the images of modes II (718 cm^{-1}), III (756 cm^{-1}), and IV (856 cm^{-1}) reveal site-specific vibrational signatures localized at the molecular center, macrocycle gaps, and isoindole lobes, respectively. Based on previous TERS studies on metal phthalocyanine molecules (e.g., ZnPc and CuPc) [59,60], mode III can be assigned to the out-of-plane bending vibration of the C–H bonds in the benzene rings, mode II is likely associated with a horizontal torsional vibration of the central macrocycle, while mode IV involves an out-of-plane twisting vibration of the benzene rings. Notably, a line profile extracted from the 756 cm^{-1} TERS mapping image yields a full width at half maximum (FWHM) of 0.43 and 0.46 nm across two lobes, suggesting an ångström scale resolution of TERS measurements (More discussion refers to SI) that is comparable to recent research.[12,61–63]

Consequently, the multimodal characterization of the AgPc molecule confirms that our cryogen-free platform achieves ångström-scale spectroscopic resolution and long-term stability required to resolve chemical fingerprints within highly localized sub-molecular regions. Moreover, this performance establishes a robust foundation for routine single-molecule and single-atom chemical imaging.

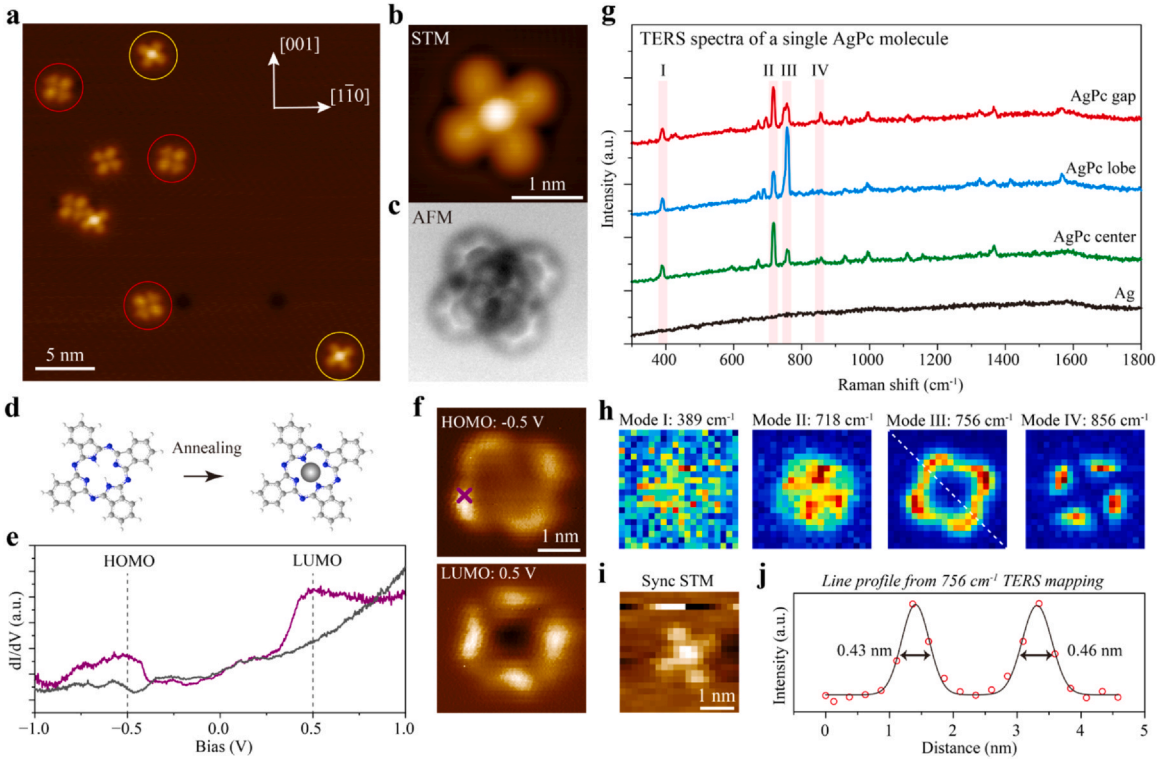

Fig. 8. Multimodal characterization of AgPc/Ag(110). (a) Large-scale STM image of H_2Pc/Ag(110) after annealing, the red and yellow rings circled out the deprotonated H_2Pc and self-metalated AgPc molecules, respectively. I_t = 200 pA, V_{bias} = 0.1 V. (b, c) High-resolution STM and nc-AFM images of a single AgPC molecule. The images were obtained by an AFM sensor with a CO-functionalized W tip, I_t = 200 pA, V_{bias} = 0.1 V, AFM oscillation amplitude = 160 pm. (d) Schematic of self-metalation reaction. (e) STS spectra recorded on the bare Ag(110) surface (grey) and the AgPc lobe (purple). I_t = 200 pA, V_{bias} = 0.1 V, V_{mod} = 5 mV, f_{mod} = 973 Hz. (f) dI/dV mapping of HOMO and LUMO states. I_t = 4 nA, V_{mod} = 20 mV, f_{mod} = 973 Hz. (g) TERS spectra (5 nA, 0.1 V, 40 s) acquired on the AgPc gap (red), lobe (blue), center (green), and bare Ag surface (black). (h) TERS mapping (3.5 × 3.5 nm^2) of vibrational modes at 389, 718, 756, and 856 cm^{-1} (I_t = 6 nA, V_{bias} = 0.1 V, 20 × 20 pixels, t_{acq} = 2 s/pixel). (i) Constant current STM image acquired simultaneously with TERS mapping. (j) Intensity line profile from 756 cm^{-1} TERS mapping image. All the TERS signals were acquired with a chemically etched Ag tip. A 0.5-mW laser (532 nm, Crystalaser, CL532–025–SO) was used to excite Raman scattering.

4. Conclusions

In summary, we have developed a cryogen-free LT-OC-SPM employing a remote liquefaction scheme that effectively mitigates vibration inherent in conventional closed-cycle setups. Our system achieves a stable base temperature of 2.78 K and a tunneling current noise level below 20 fA/Hz$^{1/2}$, matching the noise performance of liquid-helium-based SPM systems while maintaining lower, more consistent temperatures. Beyond eliminating logistical and helium-supply challenges, this cryogen-free system enables uninterrupted, months duration operation and continuous data acquisition, significantly boosting experimental throughput. By integrating a custom scanner with in-vacuo nano-positioner-driven high-NA optics, our system facilitates synergistic STM, nc-AFM, STS, STML, and TERS measurements. The multimodal characterization of AgPc/Ag(110) demonstrates this capability, providing ångström-scale insights into atomic structures and localized vibrational modes. Ultimately, the long-term stable operation of this cryogen-free SPM provides an exceptional and steady platform for time-consuming experiments under complex, extreme conditions.

Author contributions

Ma R, Huan Q, and Li H designed the SPM system. Liu D, Shi C and Huang Y built the system and performed the experiments of the cooling-down test, PSD measurement, the STM and AFM experiments on Au (111) under the supervision of Huan Q; Liu L and Tao J developed the current amplifier and the AFM amplifier; Liu Z performed the STM, STS, AFM and TERS measurements of AgPc on Ag(110) under the supervision of Tan S, Wang B and Dong Z; Liu D drafted the manuscript and revised it in consultation with all authors.

Declaration of Competing Interest

The authors declare that they have no known competing financial interests or personal relationships that could have appeared to influence the work reported in this paper.

Acknowledgement

This work was supported by the National Science Fund for Distinguished Young Scholars (T2125014, 22425206), Beijing Natural Science Foundation (L245001), National Key Research and Development Program of China (2024YFF0727100, 2025YFF1501200, 2024YFA1409800), Scientific Research Instrument and Equipment Development Project of CAS (PTYQ2024TD0011, PTYQ2024BJ0005), National Natural Science Foundation of China (92577202), the CAS Project for Young Scientists in Basic Research (YSBR-054), and Quantum Science and Technology-National Science and Technology Major Project (2021ZD0303302).

Appendix A. Supporting information

Supplementary data associated with this article can be found in the online version at doi:10.1016/j.asi.2026.100011.

References

1. Bian K, Gerber C, Heinrich AJ, Müller DJ, Scheuring S, Jiang Y. Scanning probe microscopy. *Nat Rev Methods Prim.* 2021;1(1):36.
2. Binnig G, Rohrer H, Gerber C, Weibel E. Tunneling through a controllable vacuum gap. *Appl Phys Lett.* 1982;40(2):178–180.
3. Giessibl FJ. Atomic resolution of the silicon (111)-(7×7) surface by atomic force microscopy. *Science.* 1995;267(5194):68–71.
4. Shang J, Wang Y, Chen M, et al. Assembling molecular Sierpiński triangle fractals. *Nat Chem.* 2015;7(5):389–393.
5. Wolf EL. Principles of electron tunneling spectroscopy. *Int Monogr Ph.* 2012.
6. Eigler DM, Schweizer EK. Positioning single atoms with a scanning tunnelling microscope. *Nature.* 1990;344(6266):524–526.
7. Itoh T, Procházka M, Dong Z-C, et al. Toward a new era of SERS and TERS at the nanometer scale: From fundamentals to innovative applications. *Chem Rev.* 2023;123(4):1552–1634.
8. Höppener C, Aizpurua J, Chen H, et al. Tip-enhanced Raman scattering. *Nat Rev Methods Prim.* 2024;4(1):47.
9. Jiang N, Foley ET, Klingsporn JM, et al. Observation of multiple vibrational modes in ultrahigh vacuum tip-enhanced Raman spectroscopy combined with molecular-resolution scanning tunneling microscopy. *Nano Lett.* 2012;12(10):5061–5067.
10. Zhang R, Zhang Y, Dong ZC, et al. Chemical mapping of a single molecule by plasmon-enhanced Raman scattering. *Nature.* 2013;498(7452):82–86.
11. Zhu L-Y, Han Y, Zhang Y-F, et al. Algorithm-assisted structure identification of individual nucleobases in single DNA chains through tip-enhanced Raman spectromicroscopy. *JACS Au.* 2025;5(10):4835–4844.
12. Xu J, Zhu X, Tan S, et al. Determining structural and chemical heterogeneities of surface species at the single-bond limit. *Science.* 2021;371(6531):818–822.
13. Li L, Schultz JF, Mahapatra S, Lu Z, Zhang X, Jiang N. Chemically identifying single adatoms with single-bond sensitivity during oxidation reactions of borophene. *Nat Commun.* 2022;13(1):1796.
14. Li L, Mahapatra S, Schultz JF, Zhang X, Jiang N. Single-molecule spectroscopic probing of n-heterocyclic carbenes on a two-dimensional metal. *Chem.* 2025;11(1).
15. Imada H, Miwa K, Imai-Imada M, Kawahara S, Kimura K, Kim Y. Real-space investigation of energy transfer in heterogeneous molecular dimers. *Nature.* 2016;538(7625):364–367.
16. Zhang Y, Luo Y, Zhang Y, et al. Visualizing coherent intermolecular dipole–dipole coupling in real space. *Nature.* 2016;531(7596):623–627.
17. Grewal A, Imada H, Miwa K, et al. Single-molecule phosphorescence and intersystem crossing in a coupled exciton plasmon system. *ACS Nano.* 2025;19(26):23796–23805.
18. Wu Y, Li B, Zhu X, et al. Polaron superlattices in n-doped single conjugated polymers. *Nat Nanotech.* 2025;20(11):1580–1587.
19. Li L, Schultz JF, Mahapatra S, et al. Angstrom-scale spectroscopic visualization of interfacial interactions in an organic/borophene vertical heterostructure. *J Am Chem Soc.* 2021;143(38):15624–15634.
20. de Campos Ferreira RC, Sagwal A, Doležal J, et al. Resonant tip-enhanced Raman spectroscopy of a single-molecule Kondo system. *ACS Nano.* 2024;18(20):13164–13170.
21. Sheng S, Wu J-B, Cong X, et al. Raman spectroscopy of two-dimensional borophene sheets. *ACS Nano.* 2019;13(4):4133–4139.
22. Liu S, Müller M, Sun Y, et al. Resolving the correlation between tip-enhanced resonance Raman scattering and local electronic states with 1 nm resolution. *Nano Lett.* 2019;19(8):5725–5731.
23. Liu D, Li L, Jiang N. Nanoscale chemical probing of metal-supported ultrathin ferrous oxide via tip-enhanced Raman spectroscopy and scanning tunneling microscopy. *Chem Biomed Imaging.* 2024;2(5):345–351.
24. Bao Y-F, Zhu M-Y, Zhao X-J, Chen H-X, Wang X, Ren B. Nanoscale chemical characterization of materials and interfaces by tip-enhanced Raman spectroscopy. *Chem Soc Rev.* 2024;53(20):10044–10079.
25. Sheng S, Li W, Gou J, Cheng P, Chen L, Wu K. Low-temperature, ultrahigh-vacuum tip-enhanced Raman spectroscopy combined with molecular beam epitaxy for in situ two-dimensional materials' studies. *Rev Sci Instrum.* 2018;89(5):053107.
26. Iwaya K, Yokota M, Hanada H, et al. Externally-triggerable optical pump-probe scanning tunneling microscopy with a time resolution of tens-picosecond. *Sci Rep.* 2023;13(1):818.
27. Peis L, He G, Jost D, Rager G, Hackl R. Polarized tip-enhanced Raman spectroscopy at liquid He temperature in ultrahigh vacuum using an off-axis parabolic mirror. *Rev Sci Instrum.* 2023;94(6):063701.
28. Cheng B, Wu D, Bian K, et al. A qPlus-based scanning probe microscope compatible with optical measurements. *Rev Sci Instrum.* 2022;93(4):043701.
29. Peña Román RJ, Auad Y, Grasso L, et al. Design and implementation of a device based on an off-axis parabolic mirror to perform luminescence experiments in a scanning tunneling microscope. *Rev Sci Instrum.* 2022;93(4):043704.
30. Pozzi EA, Goubert G, Chiang N, et al. Ultrahigh-vacuum tip-enhanced Raman spectroscopy. *Chem Rev.* 2017;117(7):4961–4982.
31. He G, Wei Z, Feng Z, et al. Combinatorial laser molecular beam epitaxy system integrated with specialized low-temperature scanning tunneling microscopy. *Rev Sci Instrum.* 2020;91(1):013904.
32. Lee J, Crampton KT, Tallarida N, Apkarian VA. Visualizing vibrational normal modes of a single molecule with atomically confined light. *Nature.* 2019;568(7750):78–82.
33. Wu Z-B, Gao Z-Y, Chen X-Y, et al. A low-temperature scanning probe microscopy system with molecular beam epitaxy and optical access. *Rev Sci Instrum.* 2018;89(11):113705.
34. Elrod SA, de Lozanne AL, Quate CF. Low-temperature vacuum tunneling microscopy. *Appl Phys Lett.* 1984;45(11):1240–1242.
35. Meyer G. A simple low-temperature ultrahigh-vacuum scanning tunneling microscope capable of atomic manipulation. *Rev Sci Instrum.* 1996;67(8):2960–2965.
36. Behler S, Rose MK, Dunphy JC, Ogletree DF, Salmeron M, Chapelier C. Scanning tunneling microscope with continuous flow cryostat sample cooling. *Rev Sci Instrum.* 1997;68(6):2479–2485.
37. Stipe BC, Rezaei MA, Ho W. A variable-temperature scanning tunneling microscope capable of single-molecule vibrational spectroscopy. *Rev Sci Instrum.* 1999;70(1):137–143.
38. Zhao Z, Wang C. *Cryogenic engineering and technologies: Principles and applications of cryogen-free systems.* CRC Press; 2019.
39. Zhang S, Huang D, Wu S. A cryogen-free low temperature scanning tunneling microscope capable of inelastic electron tunneling spectroscopy. *Rev Sci Instrum.* 2016;87(6):063701.

40. Hackley JD, Kislitsyn DA, Beaman DK, Ulrich S, Nazin GV. High-stability cryogenic scanning tunneling microscope based on a closed-cycle cryostat. *Rev Sci Instrum.* 2014;85(10):103704.
41. Huang H, Shuai M, Yang Y, et al. Cryogen free spin polarized scanning tunneling microscopy and magnetic exchange force microscopy with extremely low noise. *Rev Sci Instrum.* 2022;93(7):073703.
42. Kasai J, Koyama T, Yokota M, Iwaya K. Development of a near-5-kelvin, cryogen-free, pulse-tube refrigerator-based scanning probe microscope. *Rev Sci Instrum.* 2022;93(4):043711.
43. Coe AM, Li G, Andrei EY. Cryogen-free modular scanning tunneling microscope operating at 4-K in high magnetic field on a compact ultra-high vacuum platform. *Rev Sci Instrum.* 2024;95(8):083702.
44. Ma R, Li H, Shi C, et al. Development of a cryogen-free sub-3 K low-temperature scanning probe microscope by remote liquefaction scheme. *Rev Sci Instrum.* 2023;94(9):093701.
45. Pan SH, Hudson EW, Davis JC. ^{3}He refrigerator based very low temperature scanning tunneling microscope. *Rev Sci Instrum.* 1999;70(2):1459–1463.
46. Zhang C, Gao B, Chen LG, et al. Fabrication of silver tips for scanning tunneling microscope induced luminescence. *Rev Sci Instrum.* 2011;82(8):083101.
47. Horcas I, Fernández R, Gómez-Rodríguez JM, Colchero J, Gómez-Herrero J, Baro AM. WSxM: A software for scanning probe microscopy and a tool for nanotechnology. *Rev Sci Instrum.* 2007;78(1):013705.
48. Li X, Xu D, Wang W, et al. Design and construction of a 1.8 k superfluid ^{4}He system with a G-M cryocooler. *Cryogenics.* 2019;102:50–55.
49. Kazemi-Zanjani N, Vedraine S, Lagugné-Labarthet F. Localized enhancement of electric field in tip-enhanced Raman spectroscopy using radially and linearly polarized light. *Opt Express.* 2013;21(21):25271–25276.
50. Giessibl FJ, Pielmeier F, Eguchi T, An T, Hasegawa Y. Comparison of force sensors for atomic force microscopy based on quartz tuning forks and length-extensional resonators. *Phys Rev B.* 2011;84(12):125409.
51. Yang Z, Aizpurua J, Xu H. Electromagnetic field enhancement in TERS configurations. *J Raman Spectrosc.* 2009;40(10):1343–1348.
52. Li P, Ding F. Origin of the herringbone reconstruction of Au(111) surface at the atomic scale. *Sci Adv.* 2022;8(40):eabq2900.
53. Chen W, Madhavan V, Jamneala T, Crommie MF. Scanning tunneling microscopy observation of an electronic superlattice at the surface of clean gold. *Phys Rev Lett.* 1998;80(7):1469–1472.
54. Giessibl FJ. The qPlus sensor, a powerful core for the atomic force microscope. *Rev Sci Instrum.* 2019;90(1):011101.
55. Zhang Y, Meng Q-S, Zhang L, et al. Sub-nanometre control of the coherent interaction between a single molecule and a plasmonic nanocavity. *Nat Commun.* 2017;8(1):15225.
56. Niu T, Li A. Exploring single molecules by scanning probe microscopy: Porphyrin and phthalocyanine. *J Phys Chem Lett.* 2013;4(23):4095–4102.
57. Smykalla L, Shukrynau P, Zahn DRT, Hietschold M. Self-metalation of phthalocyanine molecules with silver surface atoms by adsorption on Ag(110). *J Phys Chem C.* 2015;119(30):17228–17234.
58. Sperl A, Kröger J, Berndt R. Controlled metalation of a single adsorbed phthalocyanine. *Angew Chem Int Ed.* 2011;50(23):5294–5297.
59. Yang B, Chen G, Ghafoor A, et al. Chemical enhancement and quenching in single-molecule tip-enhanced Raman spectroscopy. *Angew Chem Int Ed.* 2023;62(13):e202218799.
60. Zhang J-X, Meng Q-S, Chen G, Zhang Y, Zhang Y, Dong Z-C. Probing the vertical resolving ability of tip-enhanced Raman spectroscopy. *ACS Photonics.* 2023;10(10):3682–3690.
61. Li L, Schultz JF, Mahapatra S, Liu D, Zhang X, Jiang N. Optical spectroscopic probing and atomic visualization of the motion of n-heterocyclic carbenes on Ag(111). *ACS Nano.* 2025;19(16):15363–15370.
62. Zhang Y, Yang B, Ghafoor A, et al. Visually constructing the chemical structure of a single molecule by scanning Raman picoscopy. *Natl Sci Rev.* 2019;6(6):1169–1175.
63. Jaculbia RB, Imada H, Miwa K, et al. Single-molecule resonance Raman effect in a plasmonic nanocavity. *Nat Nanotech.* 2020;15(2):105–110.